The Astrophysical Journal, 980:88 (13pp), 2025 February 10 https://doi.org/10.3847/1538-4357/ad9d3d

Study of Long-term Spectral Evolution and X-Ray and γ-Ray Correlation of Blazars Seen by HAWC

R. Alfaro[1], C. Alvarez[2], A. Andrés[3], J.C. Arteaga-Velázquez[4], D. Avila Rojas[1], H.A. Ayala Solares[5], R. Babu[6], E. Belmont-Moreno[1], A. Bernal[3], K.S. Caballero-Mora[2], T. Capistrán[3], A. Carramiñana[7], F. Carreón[3], S. Casanova[8], U. Cotti[4], J. Cotzomi[9], S. Coutiño de León[10], E. De la Fuente[11], D. Depaoli[12], N. Di Lalla[13], R. Diaz Hernandez[7], B.L. Dingus[14], M.A. DuVernois[10], M. Durocher[14], J.C. Díaz-Vélez[10], K. Engel[15], C. Espinoza[1], K.L. Fan[15], N. Fraija[3], S. Fraija[3], J.A. García-González[16], F. Garfias[3], A. Gonzalez Muñoz[1], M.M. González[3], J.A. Goodman[15], S. Groetsch[6], J.P. Harding[14], S. Hernández-Cadena[29], I. Herzog[17], D. Huang[15], F. Hueyotl-Zahuantitla[2], A. Iriarte[3], V. Joshi[18], S. Kaufmann[19], D. Kieda[20], A. Lara[21], W.H. Lee[3], J. Lee[22], H. León Vargas[1], J.T. Linnemann[17], A.L. Longinotti[3], G. Luis-Raya[19], K. Malone[14], O. Martinez[9], I. Martinez-Castellanos[23], J. Martínez-Castro[24], J.A. Matthews[25], P. Miranda-Romagnoli[26], J.A. Montes[3], E. Moreno[9], M. Mostafá[5], A. Nayerhoda[8], L. Nellen[27], M.U. Nisa[17], R. Noriega-Papaqui[26], N. Omodei[13], M. Osorio[3], Y. Pérez Araujo[1,3], E.G. Pérez-Pérez[19], C.D. Rho[28], D. Rosa-González[7], E. Ruiz-Velasco[12], H. Salazar[9], D. Salazar-Gallegos[17], A. Sandoval[1], M. Schneider[15], J. Serna-Franco[1], A.J. Smith[15], Y. Son[22], R.W. Springer[20], O. Tibolla[19], K. Tollefson[17], I. Torres[7], R. Torres-Escobedo[29], R. Turner[6], F. Ureña-Mena[7], E. Varela[9], L. Villaseñor[9], X. Wang[6], I.J. Watson[22], K. Whitaker[5], E. Willox[15], S. Yun-Cárcamo[15], H. Zhou[29], C. de León[4],
(HAWC collaboration)
and
Abraham D. Falcone[30], and Fredric Hancock[30,31]
[1] Instituto de Física, Universidad Nacional Autónoma de México, Ciudad de Mexico, Mexico
[2] Universidad Autónoma de Chiapas, Tuxtla Gutiérrez, Chiapas, Mexico
[3] Instituto de Astronomía, Universidad Nacional Autónoma de México, Ciudad de Mexico, Mexico, magda@astro.unam.mx
[4] Universidad Michoacana de San Nicolás de Hidalgo, Morelia, Mexico
[5] Department of Physics, Temple University, Philadelphia, PA, USA
[6] Department of Physics, Michigan Technological University, Houghton, MI, USA
[7] Instituto Nacional de Astrofísica, Óptica y Electrónica, Puebla, Mexico
[8] Instytut Fizyki Jadrowej im Henryka Niewodniczanskiego Polskiej Akademii Nauk, IFJ-PAN, Krakow, Poland
[9] Facultad de Ciencias Físico Matemáticas, Benemérita Universidad Autónoma de Puebla, Puebla, Mexico
[10] Department of Physics, University of Wisconsin–Madison, Madison, WI, USA
[11] Departamento de Física, Centro Universitario de Ciencias Exactase Ingenierias, Universidad de Guadalajara, Guadalajara, Mexico
[12] Max-Planck Institute for Nuclear Physics, 69117 Heidelberg, Germany
[13] Department of Physics, Stanford University, Stanford, CA 94305-4060, USA
[14] Los Alamos National Laboratory, Los Alamos, NM, USA
[15] Department of Physics, University of Maryland, College Park, MD, USA
[16] Tecnologico de Monterrey, Escuela de Ingeniería y Ciencias, Ave. Eugenio Garza Sada 2501, Monterrey, N.L., 64849, Mexico; anteus79@tec.mx
[17] Department of Physics and Astronomy, Michigan State University, East Lansing, MI, USA
[18] Erlangen Centre for Astroparticle Physics, Friedrich-Alexander-Universität Erlangen-Nürnberg, Erlangen, Germany
[19] Universidad Politecnica de Pachuca, Pachuca, Hgo, Mexico
[20] Department of Physics and Astronomy, University of Utah, Salt Lake City, UT, USA
[21] Instituto de Geofísica, Universidad Nacional Autónoma de México, Ciudad de Mexico, Mexico
[22] University of Seoul, Seoul, Republic of Korea
[23] NASA Goddard Space Flight Center, Greenbelt, MD 20771, USA
[24] Centro de Investigación en Computación, Instituto Politécnico Nacional, México City, Mexico
[25] Department of Physics and Astronomy, University of New Mexico, Albuquerque, NM, USA
[26] Universidad Autónoma del Estado de Hidalgo, Pachuca, Mexico
[27] Instituto de Ciencias Nucleares, Universidad Nacional Autónoma de Mexico, Ciudad de Mexico, Mexico
[28] Department of Physics, Sungkyunkwan University, Suwon 16419, Republic of Korea
[29] Tsung-Dao Lee Institute & School of Physics and Astronomy, Shanghai Jiao Tong University, 800 Dongchuan Rd, Shanghai, SH 200240, People's Republic of China
[30] Pennsylvania State University, Astronomy & Astrophysics Department, University Park, PA, USA
[31] Now at University of Illinois Urbana Champaign, Department of Physics, Urbana, IL, USA
Received 2024 February 7; revised 2024 December 4; accepted 2024 December 9; published 2025 February 5

Abstract

The HAWC Observatory collected 6 yr of extensive data, providing an ideal platform for long-term monitoring of blazars in the very high energy (VHE) band, without bias toward specific flux states. HAWC continuously monitors blazar activity at TeV energies, focusing on sources with a redshift of $z \leqslant 0.3$, based on the Third Fermi-LAT Catalog of High-Energy sources. We specifically focused our analysis on Mrk 421 and Mrk 501, as they are the brightest blazars observed by the HAWC Observatory. With a data set of 2143 days, this work significantly extends the monitoring previously published, which was based on 511 days of observation. By utilizing HAWC

data for the VHE γ-ray emission in the 300 GeV–100 TeV energy range, in conjunction with Swift-XRT data for the 0.3–10 keV X-ray emission, we aim to explore potential correlations between these two bands. For Mrk 501, we found evidence of a long-term correlation. Additionally, we identified a period in the light curve where the flux was very low for more than 2 yr. On the other hand, our analysis of Mrk 421 measured a strong linear correlation for quasi-simultaneous observations collected by HAWC and Swift-XRT. This result is consistent with a linear dependence and a multiple-zone synchrotron self-Compton model to explain the X-ray and γ-ray emission. Finally, as suggested by previous findings, we confirm a harder-when-brighter behavior in the spectral evolution of the flux properties for Mrk 421. These findings contribute to the understanding of blazar emissions and their underlying mechanisms.

Unified Astronomy Thesaurus concepts: Active galactic nuclei (16); High energy astrophysics (739); Blazars (164); Gamma-ray astronomy (628); Gamma-ray detectors (630); Gamma-ray observatories (632); X-ray observatories (1819)

1. Introduction

Blazars are active galactic nuclei characterized by the presence of a relativistic jet closely aligned with the observer's line of sight, typically with estimated viewing angles of $\theta \lesssim 10^{\circ}$. These objects exhibit high variability across the entire electromagnetic spectrum. Extensive research has explored the variability in blazars, revealing both short- and long-timescale variations (M.-H. Ulrich et al. 1997; P. Romano et al. 2006; R. Falomo et al. 2014; V. A. Acciari et al. 2021).

Blazars have a spectral energy distribution (SED) that exhibits a distinctive double-peak structure. Based on the location of the synchrotron peak of the low-energy component of their SED, they can be classified into three groups: low-energy peaked BL Lac, intermediate-energy peaked BL Lac, and high-energy peaked BL Lac (P. Padovani & P. Giommi 1995). It is well established that the low-energy peak comes from synchrotron radiation generated by relativistic electrons within the jet (M.-H. Ulrich et al. 1997)

In the SEDs of blazars, a second peak in the high-energy component is observed at γ-ray energies and sometimes includes measurable TeV emission, primarily attributed to the synchrotron self-Compton (SSC) mechanism. The influence of hadronic contributions on this emission remains relatively unknown.

Correlations between TeV γ-rays and X-rays have been observed on multiple occasions, both during high-activity states or flares (D. J. Macomb et al. 1995; G. Fossati et al. 2004; J. Albert et al. 2007; M. M. González et al. 2019; V. A. Acciari et al. 2021) and during quiescent states (J. Aleksić et al. 2015a; D. Paneque et al. 2016; V. A. Acciari et al. 2021). In only a few cases, TeV γ-ray flares without a corresponding X-ray flaring emission have been detected, referred to as "orphan flares" (M. Błażejowski et al. 2005; V. A. Acciari et al. 2009).

The interpretation of correlations found between optical bands and TeV γ-rays/X-rays remains controversial. Some studies have reported optical/TeV and γ-ray/X-ray correlations, as well as noncorrelations, with different time lags (D. Horan et al. 2009; J. Aleksić et al. 2015a), while others have found no correlations at all (D. J. Macomb et al. 1995; J. Albert et al. 2007; J. Aleksić et al. 2015a). Similarly, the emission in the radio band does not typically appear to be correlated with TeV γ-rays (V. A. Acciari et al. 2011).

Detailed studies of the correlation between X-rays and TeV emissions are crucial for constraining and distinguishing between leptonic and hadronic models of the SED. Mrk 501 has been extensively investigated in both quiescent and flaring states with the aim of exploring correlations between the TeV γ-ray, X-ray, and optical bands on timescales ranging from minutes to days (M. Gliozzi et al. 2006; B. Kapanadze et al. 2017; H. Abdalla et al. 2019; K. Singh et al. 2019; A. Pandey 2020).

For example, a direct correlation between X-ray and TeV γ-ray emissions was confirmed during the years 1997, 1998, 1999, 2000, and 2004 that appeared to be stronger when the source was brighter (M. Gliozzi et al. 2006). In 2014, from March to October, there was no significant correlation between emissions in the energy band of 0.3–300 GeV and optical-UV fluxes. However, a strong correlation was found between the TeV γ-ray and X-ray during this period (B. Kapanadze et al. 2017). In a more recent study, a trend of harder-when-brighter behavior was observed for Mrk 421 (V. A. Acciari et al. 2021). However, despite the campaign spanning several years, it primarily featured low-activity periods and did not lead to a definitive conclusion.

HAWC conducts surveys of the sky to monitor blazar activity at TeV energies (A. Albert et al. 2021). For this search, HAWC utilizes the Third Fermi-LAT Catalog of High-Energy sources (M. Ajello et al. 2017), targeting sources with a redshift of $z \leqslant 0.3$. In this context, HAWC has successfully detected two of the brightest blazars, Mrk 421 and Mrk 501.

These sources were previously studied in detail in a prior work (A. U. Abeysekara et al. 2017a), where the light curves (LCs) for a total of 511 days were presented. In an attempt to identify a possible X-ray/γ-ray correlation, data from the Burst Alert Telescope (Swift-BAT) was used in the 15–50 keV band for the X-ray emission and HAWC data for the very high energy (VHE) emission were examined. However, no significant evidence of a correlation between the two bands was found. Additionally, the study reported that the average flux for Mrk 421 in the same period of time was approximately 0.8 Crab units (CU) above 1 TeV. Mrk 501 exhibited an average flux of approximately 0.3 CU above 1 TeV.

In this paper, we extend our analysis utilizing data from 2014 November to 2020 October for a total duration of 2143 days. We employ data from the *X*-Ray Telescope (Swift-XRT) in the 0.3–10 keV band for the X-ray emission.

Furthermore, if the γ-ray emission at TeV energies arises from the SSC mechanism, the corresponding synchrotron emission would occur at softer X-rays compared to what is observed by Swift-BAT. In consequence, this synchrotron emission would be closer to its peak, ranging from 0.3 to 5 keV (B. Bartoli et al. 2016), which corresponds to the energy range of Swift-XRT.

The primary objective of this work is to use data from long-term monitoring to investigate whether a correlation exists between TeV emission and soft X-ray emission. Such a correlation is a natural consequence of the SSC model as the

underlying γ-ray emission mechanism for Mrk 421 and Mrk 501. If confirmed, we can also assess the harder-when-brighter evolution of the spectrum. A detailed description of this correlation and its robustness may suggest contributions from other processes or provide insights into the emission's mechanisms, such as the number of emission zones (K. Katarzyński & K. Walczewska 2010) or whether the emission occurs in the Klein–Nishina limit (F. Tavecchio et al. 1998).

We present our results as follows. In Section 2, we provide a brief overview of the two sources of interest, including details about the observation campaigns and the results of X-ray/γ-ray correlation analysis. Section 3.1 presents an overview of the HAWC Observatory and outlines our data analysis process. Section 3.2 briefly covers the reduction of Swift-XRT data. In Section 3.4, we extend our Bayesian block (BB) analysis to the data sample of 2143 days for both Mrk 501 and Mrk 421. Section 3.3 introduces the X-ray/γ-ray correlation and outlines our methodology for assessing result robustness. In Section 4.5, we measure the γ-ray versus photon index correlation for Mrk 421. Finally, Section 5 discusses the results and conclusions obtained in this study.

2. The Sources

HAWC observes two of the brightest blazars in the northern TeV sky, which have been the focus of multiple observation campaigns. Extensive monitoring of Mrk 421 and Mrk 501 has significantly enhanced our understanding of their broadband emission, as summarized in the following two subsections.

2.1. Mrk 421

VHE emission from Mrk 421 ($z = 0.031$) was first detected by the Whipple Observatory (M. Punch 1992). Extensive monitoring campaigns have been conducted at various activity levels. Some campaigns were not restricted to specific source states and included both low and high states in the data analysis. For instance, one campaign utilized data from the Whipple 10 m telescope for the TeV γ-ray emission alongside data from the Rossi X-Ray Timing Explorer (RXTE). This campaign, conducted from 2003 to 2004 (M. Blazejowski et al. 2005), yielded valuable insights, including variability studies and a correlation between the two emissions. Notably, it revealed the occurrence of TeV flares with no counterparts at longer wavelengths. According to the authors, the analysis of these flares during that period posed challenges to both leptonic and hadronic models.

Another example of an intermediate-flux-state campaign occurred over 2 months in 2002 December and 2003 January (P. F. Rebillot et al. 2006).

Regarding low-activity states, a campaign spanning 4.5 months in 2009 (HI4PI Collaboration et al. 2016) deserves mention. During this period, when the average flux of Mrk 421 was approximately 0.5 times the flux of the Crab Nebula, the campaign successfully identified a strong X-ray/γ-ray correlation. This correlation was established using data from the RXTE Proportional Counter Array and Swift-XRT 2–10 keV for X-rays and MAGIC and Whipple for VHE γ-rays. Additionally, the campaign observed a trend of harder-when-brighter behavior in the X-ray spectra.

Multiple campaigns have been conducted to investigate high-activity states of the source. One illustrative example is a campaign during the 2006 and 2008 outburst of Mrk 421 (V. A. Acciari et al. 2009). This multiwavelength campaign incorporated UV and X-ray data from XMM-Newton along with γ-ray data from the 10 m Whipple telescope and VERITAS and MAGIC telescopes. A primary focus was to obtain simultaneous data across these three wavelengths. The 2006 data facilitated the study of source variability, while the 2008 data aimed to identify correlations between X-ray and γ-ray bands. However, the study reported no measurable correlation in the sample used.

Regarding the measurement of X-ray/γ-ray correlation at TeV energies, several analyses have identified correlations between the two bands (G. Fossati et al. 2008; V. Acciari et al. 2014; B. Bartoli et al. 2016; V. A. Acciari et al. 2021; MAGIC Collaboration et al. 2021) utilizing either GeV or TeV bands for the γ-ray emission.

In some of the aforementioned studies, evidence supports a harder-when-brighter trend for the spectra. However, it is important to note that in certain cases, this behavior cannot be extended to the highest fluxes (V. A. Acciari et al. 2021).

The HAWC Collaboration recently conducted a time-averaged analysis of the TeV SED for Mrk 421 using a data set spanning 1038 days. Their analysis revealed that the intrinsic spectrum of this source can be adequately represented by a power law with an exponential cutoff (A. Albert et al. 2022). Additionally, this analysis determined that the maximum energy at which the source is detected is 9 TeV.

In this work, we build upon previous monitoring efforts of Mrk 421 that utilized 511 days of data and initially explored the possibility of X-ray/γ-ray correlation using Swift-BAT data. However, no conclusive evidence of such correlation was found in that preliminary investigation (A. U. Abeysekara et al. 2017a). One potential explanation for the absence of correlation, as discussed in Section 1, may relate to the expectation in the SSC model that the γ-ray emission is strongly linked to a significantly softer X-ray component than that traced by Swift-BAT, which has a hard bandpass at $E > 15$ keV, therefore providing a strong motivation for the use of Swift-XRT data in these studies (B. Bartoli et al. 2016).

2.2. Mrk 501

VHE emission from Mrk 501 ($z = 0.034$) was first detected by the Whipple Observatory (J. Quinn et al. 1996).

In the study performed by M. Tluczykont et al. (2010), a comprehensive analysis covering over a decade of data collected from various experiments revealed an X-ray/γ-ray linear correlation for Mrk 501. It is important to note that the flux measurements were not strictly simultaneous, as they were averaged over 12 hr.

During an observation campaign conducted from 2011 October to November (B. Bartoli et al. 2012), the ARGO-YBJ experiment reported no significant correlation between X-ray emission in the 15–50 keV band using Swift-BAT data and γ-ray emission (>0.3 TeV). The source was also analyzed during the X-ray flaring periods, and although there was an increase in the γ-ray emission, there was no evidence of correlation with X-ray emission.

In a high-activity campaign (MAGIC Collaboration et al. 2020), a significant correlation between the two bands was reported, and this correlation appeared to increase slightly with higher X-ray energies. It is noteworthy that during the low-activity periods, the correlation weakened, and in some cases, it disappeared.

For long-term measurements, a campaign spanning over 5 yr found that the correlation remain strong and could exhibit both linear and nonlinear behaviors (M. Gliozzi et al. 2006). Additionally, the study characterized the long-term X-ray flux and spectral variability. In terms of long-term timescales, the spectrum tended to harden when the source brightened, consistent with typical blazar behavior.

Multiwavelength correlations spanning from 2012 to 2018 were also studied by A. Arbet-Engels et al. (2021), and a strong TeV/X-ray correlation with zero lag was found.

HAWC also performed a time-averaged analysis of the TeV SED for Mrk 501 (A. Albert et al. 2022), and it found that its intrinsic spectra can be represented with a simple power law. It also measured that the maximum energy at which the source is detected is 12 TeV.

It is noteworthy to mention that Mrk 501 has shown low broadband activity for an extended period of time, starting at mid-2017 and extending up to 2019, as reported by H. Abe et al. (2023), where a significant correlation between X-rays and γ-rays was also found.

3. Analysis

3.1. HAWC Data Analysis

HAWC is comprised of an array of 300 water Cherenkov detectors (WCDs), each with dimensions of 7.3 m in diameter and 4.5 m in depth (A. Abeysekara et al. 2023). The total effective area is approximately 22,000 m^2 for the 300 WCDs. Situated at an elevation of approximately 4100 m above sea level, HAWC is located on the slopes of the Sierra Negra volcano in the state of Puebla, Mexico. It has been in operation for more than 7 yr, boasting an impressive duty cycle exceeding 95%.

With an instantaneous field of view of 2 sr, HAWC surveys two-thirds of the sky every day, operating with an energy range spanning from 300 GeV to 100 TeV. One of the key advantages of the HAWC Observatory is its ability to provide continuous and unbiased monitoring, unrestricted by seasonal observing limitations. Since late 2014, it has monitored the TeV sky and accumulated a vast data sample spanning over 6 yr.

For this analysis, we utilized the same data reconstruction version as employed in A. U. Abeysekara et al. (2017a). The data set covers the period from 2014 November to 2020 October. Here, we provide only pertinent details of the adopted analysis; for a comprehensive description, please refer to A. U. Abeysekara et al. (2017a, 2017b).

In the HAWC Observatory's event recording, an HAWC event is registered when a minimum number of photomultiplier tubes (PMTs) trigger within a specified time window. These events are classified into nine distinct analysis bins (designated as $\mathcal{B}$ identifiers ranging from 1 to 9). The classification is based on the fraction of available PMTs triggered by each event (see A. U. Abeysekara et al. 2019 for detailed information). The gamma/hadron separation criteria, outlined in A. U. Abeysekara et al. (2017b), are applied from bin 1 to bin 9.

To obtain the flux normalization, we employ the daily maps in sidereal days, as explained in A. U. Abeysekara et al. (2017a), which encompass a full transit of a given source within the R.A. range of $45^\circ <$ R.A. $< 315^\circ$. These daily maps were utilized for daily monitoring of blazars such as Mrk 421, Mrk 501, and the Crab Nebula (A. U. Abeysekara et al. 2017a) and covered 511 days of data. Notably, the sources of interest transit the sky above HAWC for approximately 6.2 hr each sidereal day. To ensure accuracy in the flux normalization, we impose a minimum coverage requirement of 50% of the transit, along with a condition that the zenith angle θ is less than 45°. Additionally, a quality cut entails the removal of subruns with a rate deviation exceeding 10σ from the sinusoidal fit to the rate within a 12 hr time window.

In cases where the coverage of a source transit is interrupted due to various circumstances, such as detector downtime, the quantification of signal loss in comparison to a full transit is determined by excluding the gap period from the integration over zenith angles (A. U. Abeysekara et al. 2017a). Subsequently, the expected event count is adjusted accordingly. One limitation of this approach is its dependency on the decl., which requires the assumption of a minimum exposure equivalent to one full transit of the source. Consequently, this method may pose challenges when attempting to obtain results involving timescales of hours, such as intraday variability studies or the observation of spectral hardening during periods of high activity, which are characteristic of γ-ray flares in blazars, as in our case of study.

One significant difference between the present work and the methods described in A. U. Abeysekara et al. (2017a) is the software employed for calculating the flux normalization. Instead of using the Likelihood Fitting Framework (LiFF; P. W. Younk et al. 2015) to obtain the flux normalization, we adopt the Zenith Band Response Analysis (ZEBRA; I. Martinez-Castellanos 2019), which is the latest software used for generating LCs in HAWC analyses and offers several improvements.

LiFF relies on assumed spectra for a given source, convolving them with a detector response function that includes the point-spread function. It subsequently employs the log-likelihood function to calculate the likelihood ratio test between a null hypothesis, assuming background only, and an alternative hypothesis that uses the input flux for the source.

In contrast, ZEBRA (I. Martinez-Castellanos 2019) determines the detector response's dependence on the zenith angle by means of simulation. This response is then convolved with the source's spectrum to estimate the observed counts over a specified time period. Importantly, ZEBRA eliminates the constraint of requiring a minimum exposure equivalent to one full transit.

A consistency check between both software packages was conducted for the Crab Nebula and the blazars Mrk 421 and Mrk 501 in J. A. Garcìa-González (2019).

We employ direct integration (R. Atkins et al. 2003) to derive a background estimate. In this procedure, a local efficiency map is constructed by averaging counts within a strip of pixels spanning 24 hr in R.A. around any given location. Subsequently, this efficiency map is smoothed using a spline fit to mitigate the limitations posed by limited statistics in higher analysis bins.

To prevent any bias in the results, pixels near the strongest known sources and the galactic plane are excluded during the averaging process. This exclusion is necessary to avoid counting γ-ray events as part of the background. The estimated background counts for each pixel are then stored in a second map.

We consider for both sources, Mrk 421 and Mrk 501, the spectral model as a power law with an exponential cutoff given

Table 1
Parameters Used in the Cutoff Power Law for the Observed Spectra of Mrk 421 and Mrk 501

Source	E_0 (TeV)	α	E_c (TeV)
Mrk 421	1	2.2	5
Mrk 501	1	1.6	6

as

$$\frac{dN}{dE} = N_0\left(\frac{E}{E_0}\right)^{-\alpha}\exp\left(\frac{E}{E_c}\right). \quad (1)$$

Here, N_0 ($\mathrm{TeV}^{-1}\,\mathrm{cm}^{-2}\,\mathrm{s}^{-1}$) represents the flux normalization, α is the photon index, and E_c (TeV) is the energy cutoff. A detailed study conducted by HAWC that takes into account the extragalactic background light absorption can be found in A. Albert et al. (2022).

In Equation (1), the parameters E_0 (TeV) (pivot energy) and α were fixed, with only the normalization N_0 as a free parameter. The specific values used for each source are summarized in Table 1 and can be found in detail in A. U. Abeysekara et al. (2017a).

The systematic uncertainties related to the calculation of the flux normalization have been extensively discussed by A. U. Abeysekara et al. (2017b). The resulting uncertainty on individual flux values under spectral hardening or softening was obtained using simulated γ-ray fluxes with different spectral parameter values. The range used for the spectral index was 2.0–2.4 and 1.2–2.0 for Mrk 421 and Mrk 501, respectively, resulting in a value of $\pm 5\%$. In the case of Mrk 421, the spectral index range can vary outside of the range presented here, as described in MAGIC Collaboration et al. (2021; from 1.95 to 2.80). For Mrk 501, the range can also include values from 2.35 to 2.67 (H. Abe et al. 2023). Other notable sources of uncertainty are the charge resolution, angular resolution, and late light simulation, the last one being the most significant contributor to uncertainty, with a maximum impact of up to 40%.

3.2. Swift-XRT Data Analysis

Swift-XRT (D. N. Burrows et al. 2005) is an X-ray telescope on board the Neil Gehrels Swift Observatory (N. Gehrels et al. 2004). Swift-XRT observations of both Mrk 421 and Mrk 501 were conducted in two different modes: the window timing (WT) mode and the photon counting (PC) mode. The majority of the observations were carried out in the WT mode due to the high count rates, which can lead to photon pileup in the PC mode.

For this study, the Swift data analyzed for both Mrk 421 and Mrk 501 span from 2014 November to 2020 October. The Swift data were binned to match the time period of a sidereal day, corresponding to HAWC data.

Data products were extracted using tools from HEASoft.[32] Initially, the cleaned level 3 event files were separated into individual snapshots, each representing a pointed observation. An image was extracted for each snapshot within the energy range of 0.3–10 keV.

In the WT mode, the first 150 s of data were discarded from each observation to exclude data affected by spacecraft settling issues. Pileup correction was applied using the method described in P. Romano et al. (2006). For the spectrum extraction, a 40 × 20 pixel ($2\farcs36\,\mathrm{pixel}^{-1}$) box was chosen as the source extraction region, and an annular boxed region with dimensions of 100 × 20 pixels was used for background spectrum extraction.

In the PC mode, a circular source region with a typical size of 20 pixels and a surrounding annular background region with inner and outer radii of typically 40 and 80 pixels, respectively, were selected for spectrum extraction. The size was dynamically chosen as a function of source count rate in the region. If the count rate is above the pileup threshold, then an annular source region is used. This pileup correction was applied when the source counts exceeded 0.6 counts s^{-1}. For a further description of these methods, refer to M. C. Stroh & A. D. Falcone (2013). Specifically, an annular region in the center of the source region was excluded to eliminate pileup affected pixels, with this annular region increasing in size for higher count rates until the pileup becomes negligible, below the 0.6 count s^{-1} threshold, outside of the central annulus ring. Subsequently, a point-spread function correction was applied based on these regions, including the correction for the chosen annulus.

All spectra were binned using 1 sidereal day intervals. Model fitting was performed using XSPEC[33] ver. 11 (Arnaud 1996) with a model consisting of a log parabola (logpar) combined with Galactic absorption as specified in the Tuebingen–Boulder Interstellar medium (ISM) absorption model (tbabs). The final model took the form *cflux*tbabs*logpar*. The *cflux* component provides the unabsorbed flux from each source in the energy band of 0.3−10 keV. The hydrogen column density along the line of sight of the two blazars was fixed at $1.9\times10^{20}\,\mathrm{cm}^{-2}$ for Mrk 421 and $1.7\times10^{20}\,\mathrm{cm}^{-2}$ for Mrk 501. These values were obtained using the HEASoft tool called the hydrogen density column calculator (HI4PI Collaboration et al. 2016).[34]

3.3. X-Ray/γ-Ray Correlation

After obtaining the γ-ray and X-ray fluxes as described in Sections 3.1 and 3.2, we employ the maximum-likelihood method, as discussed in G. D'Agostini (2005, 2003), to assess the linear correlation between them. This method allows us to not only determine the strength of the correlation but also measure the degree of dispersion in the data using the parameter σ_d.

The underlying assumption of this method is that when the correlated data pair (F_x^i, F_γ^i) follows a linear dependence $F_\gamma = aF_x + b$ with an intrinsic scatter σ_d, we can derive the optimal values of the parameters (a, b, and σ_d) using the likelihood function. This function takes into account the uncertainties with F_x^i and F_γ^i ($\sigma_{F_x^i}$ and $\sigma_{F_\gamma^i}$, respectively) within its calculations and can be expressed as follows:

$$L(a, b, \sigma_d) = \frac{1}{2}\sum_i \log(\sigma_d^2 + \sigma_{F_\gamma^i}^2 + a\sigma_{F_x^i}^2) + \frac{1}{2}\sum_i \frac{(F_{\gamma^i}^2 - aF_{x^i}^2 - b^2)^2}{\sigma_d^2 + \sigma_{F_\gamma^i}^2 + a\sigma_{F_x^i}^2}. \quad (2)$$

This approach allows us to rigorously assess the correlation between the γ-ray and X-ray fluxes, considering both their values and associated uncertainties.

[32] https://heasarc.gsfc.nasa.gov/docs/software/lheasoft/

[33] https://heasarc.gsfc.nasa.gov/xanadu/xspec/

[34] https://heasarc.gsfc.nasa.gov/cgi-bin/Tools/w3nh/w3nh.pl

3.4. BBs

To assess the origin of the intrinsic dispersion σ_d, we also evaluate the flux correlation by segmenting the data into BBs that represent periods of time where the flux is consistent with being constant within the statistical uncertainties. In this case, we apply the BB algorithm to the HAWC fluxes and combine the X-ray fluxes accordingly.

We utilized the "point measurements fitness function" for the BB algorithm, as outlined in Section 3.3 of J. D. Scargle et al. (2013), to analyze the daily flux data in the γ-ray LCs.

To apply this algorithm effectively, an initial Bayesian prior, denoted as $ncp_{\rm prior}$, must by chosen. The probability of encountering a new transition in flux state is determined by this prior, where $\gamma = \exp^{-ncp_{\rm prior}}$ represents the constant factor that quantifies the likelihood of detecting $k+1$ transition points as opposed to k points (i.e., the likelihood of a false positive). It is important to note that the choice of $ncp_{\rm prior}$ depends on factors such as the length of the LC and the uncertainties associated with the flux measurements. The values of the constant flux amplitude that represent the flux at each block, which are defined by the position of the change points, are obtained by calculating the averages of the corresponding daily measurements, weighted by the inverse square of the individual flux uncertainties (A. U. Abeysekara et al. 2017a).

To address this sensitivity to different data conditions, we performed simulations of the source's flux by generating synthetic LCs spanning the same number of days as in the available data.

We conducted simulations of LCs by introducing Poissonian fluctuations based on background maps around the coordinates of the sources of interest. Additionally, we injected a Crab-like point source targeting an average flux of 1 CU. It is worth noting that our simulation approach differs from the one employed in the HAWC monitoring, which was previously used to generate blazar LCs (A. U. Abeysekara et al. 2017a). In the previous method, a constant flux hypothesis was utilized, following a Gaussian distribution with a standard deviation consistent with the measured uncertainty in the data for the sources of interest.

For our simulations, we set a false-positive rate (FPR) of 5%, indicating the probability of detecting at least one additional flux transition beyond the one corresponding to the injected base flux.

We determined the HAWC flux for each BB by treating the normalization N_0 and the photon index α as free parameters. This approach is feasible due to the significant signal-to-background ratio observed in the majority of the BBs, which allows for constraints on both parameters.

4. Results and Discussion

4.1. LCs

For Mrk 421 and Mrk 501, we calculated the γ-ray flux >1 TeV for each HAWC transit, which has a duration of approximately 6.2 hr, and the corresponding X-ray flux in the 0.3–10 keV energy band using the data and software detailed in Sections 3.1 and 3.2, respectively. The resulting γ-ray and X-ray LCs are presented in Figure 1. In this figure, we only display X-ray fluxes that overlap in time with HAWC observations for Mrk 501 and Mrk 421, which amount to 3 and 74 data points, respectively. We have highlighted in red all the daily fluxes with a significance below 2σ. In the case of Mrk 501, we have an integrated flux distribution dominated by low significance values, which also leads to negative flux values. We checked the significance distribution for the source and also in the case when there is only a background expectation, and we found them to be consistent with each other. The significance distributions are centered at zero, and they are not fully Gaussian, showing a broader distribution with an average standard deviation of ~ 1.5 σ. This leads to higher statistical fluctuations to more extreme significance values as expected for a Gaussian distribution.

Mrk 501 exhibited low activity during the majority of the observational period, spanning over 2 yr. However, there was an initial burst of activity between 2015 January and June, during which both the γ-ray and the X-ray fluxes increased by a factor of approximately 5 and 3, respectively. A brief flare is discernible around 2016 April with X-ray and γ-ray emissions, the former seemingly lasting longer than the latter.

In contrast, Mrk 421 displayed several periods of heightened activity in both energy bands. The highest X-ray fluxes occurred between 2018 January and April, while the highest γ-ray fluxes, equivalent to ~7 CU, were observed toward the end of the HAWC observational period, after 2020 June. Notably, Mrk 421 appears to be active simultaneously in both energy bands. It is worth mentioning that during the period after 2020 June, the LC exhibits four distinct peaks, each lasting approximately 15 days. A more detailed analysis of these flares is planned for future studies.

4.2. X-Ray/γ-Ray Correlation per Transit

To investigate the presence of a correlation between the emissions in both energy bands, we adopt the procedure outlined in Section 3.3 and start with the simplest model: a linear correlation. This choice is motivated, particularly for Mrk 421, by previous studies conducted in similar energy bands, for example, M. Amenomori et al. (2003), M. Błażejowski et al. (2005), M. M. González et al. (2019), and V. A. Acciari et al. (2020).

To calculate the X-ray/γ-ray correlation, we use the HAWC transits that have a corresponding X-ray flux; then we are only considering the remaining transits when a minimum of 2σ for the γ-ray flux significance is reached.

The results of the correlation for both sources are presented in Figure 2 (panels (a) and (b)), and, in the case of Mrk 421, the values of the parameters are summarized in Table 2 (first row). For Mrk 501, we only obtained three data points; therefore, we cannot obtain a reliable measurement for the correlation per transit.

We also search for cross-correlation between the two bands to investigate weather a time lag between the γ-rays and X-rays was present. We used the discrete correlation function (R. A. Edelson & J. H. Krolik 1988) as implemented in D. R. S. Robertson et al. (2015). The result for Mrk 421 is shown in Figure 2(c); we obtain a correlation of 0.84 ± 0.13 with no time lag. A similar study (V. A. Acciari et al. 2021) that used multiwavelength data from a campaign spanning from 2015 to 2016 also found a strong correlation with no time lag between VHE γ-rays and X-rays using data from MAGIC (two energy bands, 0.2–1 TeV and >1 TeV) and FACT ($E_{\rm th}$ ~ 0.7 TeV) for the VHE emission and data from Swift-XRT (0.3–10 keV) for the X-ray emission. Additionally, in our work for Mrk 501 (Figure 2(d)), there is no evidence of correlation.

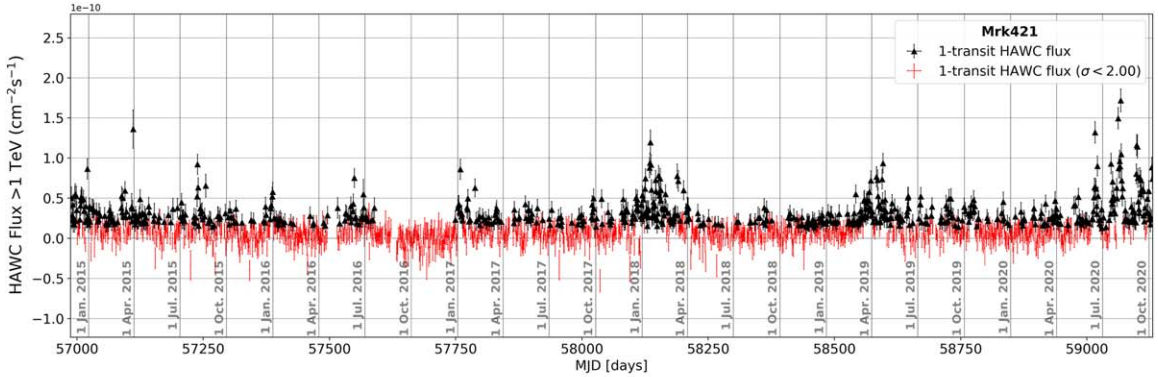

(a)

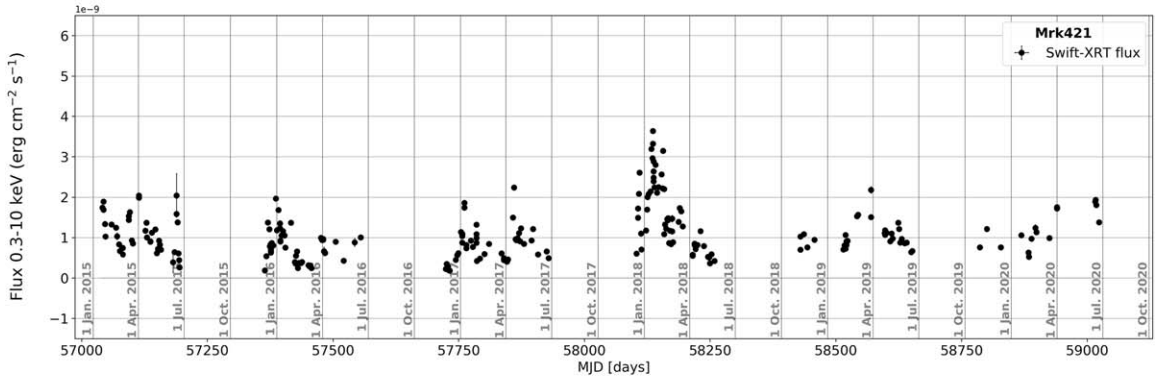

(b)

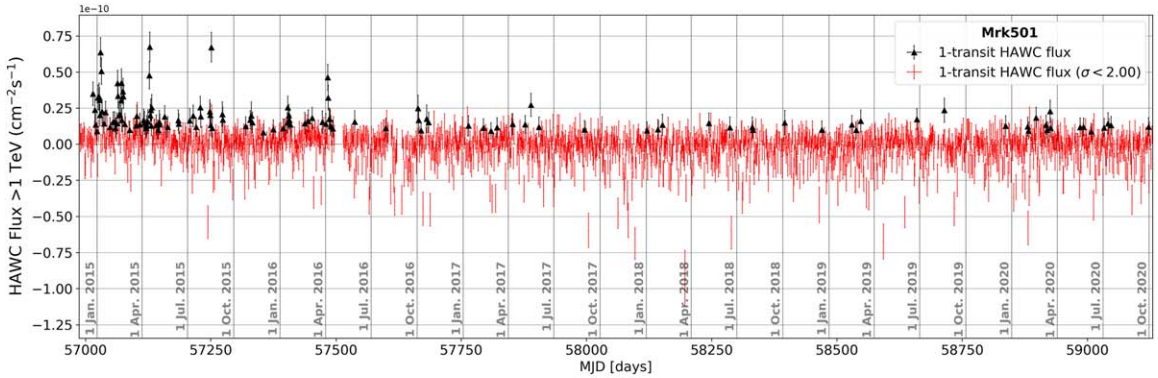

(c)

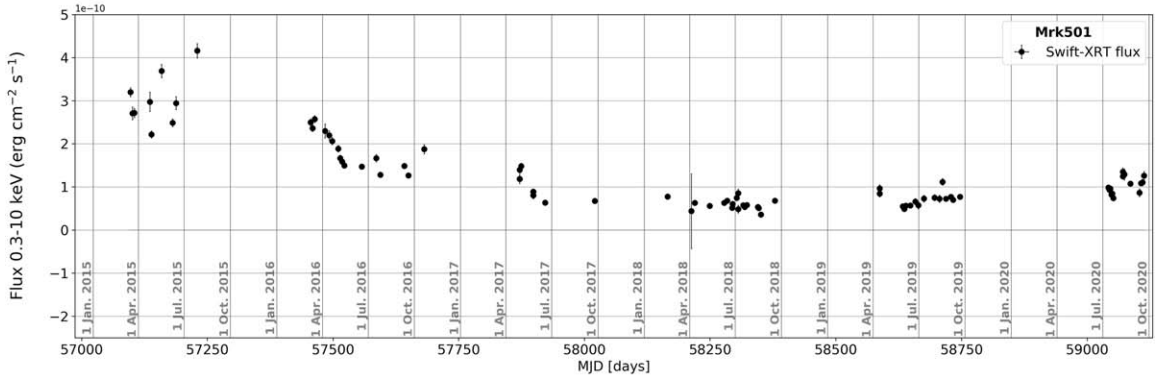

(d)

Figure 1. LCs for Mrk 421 and Mrk 501. HAWC LC showing Integrated flux >1 TeV (panels (a) and (c)). A red marker is shown when the significance in the flux was below 2σ for that transit. For the Swift-XRT LC (panels (b) and (d)), showing integrated flux between 0.3 and 10 keV.

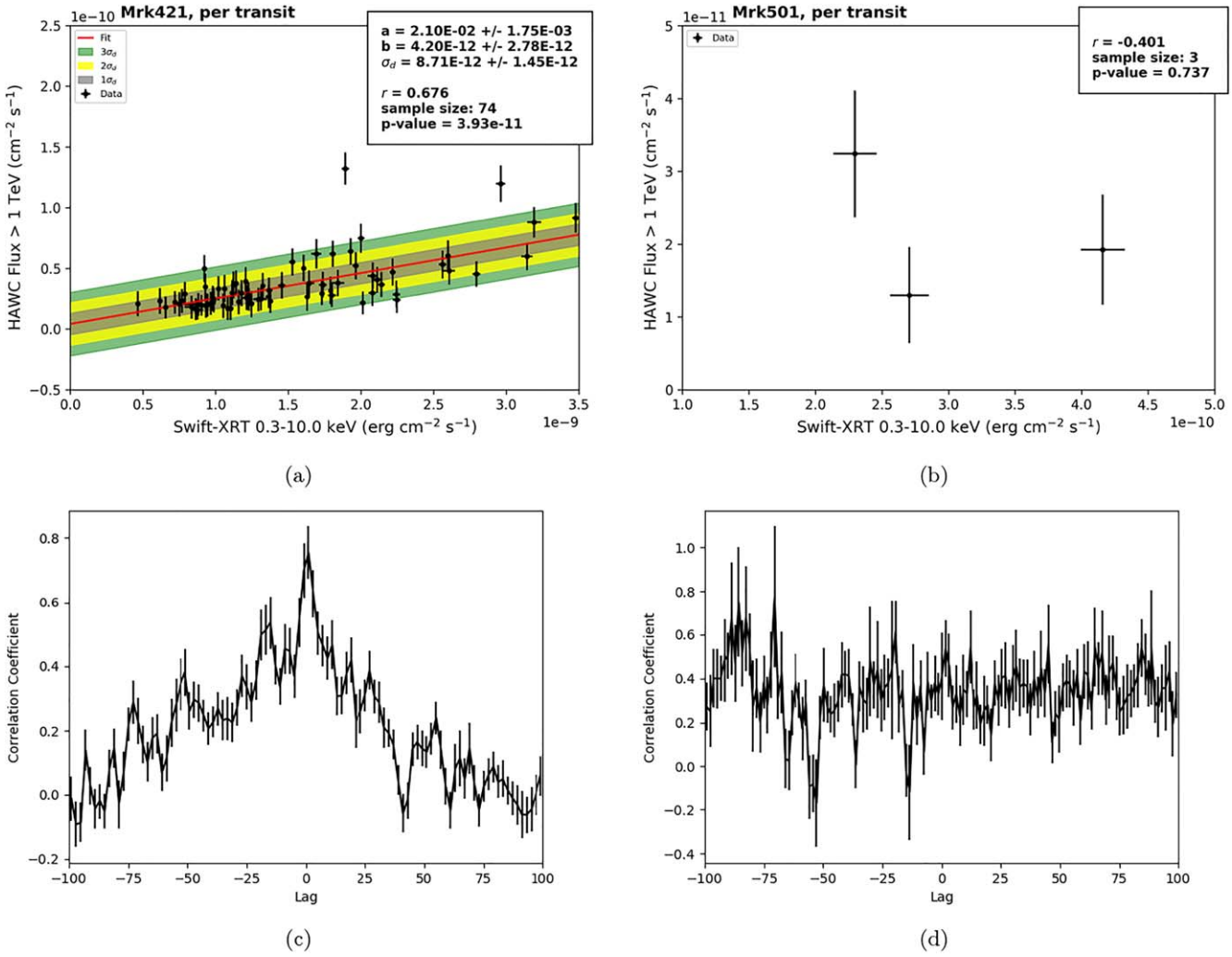

Figure 2. X-ray/γ-ray correlation for Mrk 421 per transit (a). The p-value of the correlation is 0.676, which shows consistency with a linear correlation. X-ray/γ-ray correlation for Mrk 501 per transit (b). It has been noticed that Mrk 501 has had a long period of very low activity that is reflected in a low flux measured even when higher activity in the X-ray emission happens, resulting in only three data points as mentioned in Section 4.2. Discrete correlation function for Mrk 421 (c). We can see a correlation between the two bands for no time lag. In the case of Mrk 501 (d), there is no evidence of correlation.

Table 2
Correlation Fit Parameters for both Mrk 421 and Mrk 501

Source	a ($\times 10^{-2}$)	b ($\times 10^{-12}$ cm^{-2}s^{-1})	σ_d ($\times 10^{-12}$ cm^{-2}s^{-1})	r	Sample Size	p-value
Mrk 421	2.10 ± 0.17	4.21 ± 2.78	8.72 ± 1.45	0.676	74	3.93×10^{-11}
Mrk 421	2.04 ± 0.15	-6.87 ± 1.90	5.27 ± 0.79	0.892	25	2.05×10^{-9}
Mrk 501	3.07 ± 0.34	-1.87 ± 0.49	0	0.947	5	1.46×10^{-2}
Mrk 421	$-3.07 \pm 0.42 \times 10^{-11}$	99.7 ± 10.3	10.7 ± 1.4	-0.686	37	2.76×10^{-6}

Note. Using the G. D'Agostini (2005) approach in Equation (2) to estimate the robustness of the linear fit by introducing an extra scatter parameter σ_d. Data used in the fit correspond to quasi-simultaneous observations of HAWC and Swift-XRT. The binning used is one HAWC transit (first row) and BBs (second and third rows). The sample size is the number of sidereal days or BBs that overlap for both data samples. The fourth row corresponds to the flux vs. photon index correlation for Mrk 421 (Figure 5).

In the case of Mrk 421, there are a few outliers where the highest γ-ray fluxes are much higher than the values predicted by the correlation for that given value of X-ray flux. Surprisingly, this does not seem to significantly affect the Pearson correlation coefficient (PCC) value, considering the obtained p-value and the size of the sample. However, even with the introduction of σ_d, it does not fully account for the dispersion observed beyond the correlation of these outliers. These results do not provide a clear explanation for whether the correlation breaks down for γ-ray fluxes beyond a value of around 1×10^{-10} cm^{-2} s^{-1} for energies greater than 1 TeV, or if there are specific activity states where either the X-ray flux is suppressed or contributions from other processes affect the γ-ray flux. It is also possible that these observations result from the quasi-simultaneity of the data and the high variability of the source. HAWC fluxes are measured over extended periods of hours, whereas Swift observations coincide with HAWC but last on the order of 1 ks. If this were the case, we should expect

to observe high X-ray fluxes alongside γ-ray fluxes that are lower than expected. However, this is not observed in at least this data set.

4.3. X-Ray/γ-Ray Correlation in BBs

The large fluctuations in the data around the correlation may have various origins. These fluctuations could result from observational statistical uncertainties, be intrinsic to the emission mechanisms, or be influenced by the quasi-simultaneity of the data. To investigate the origin of the fluctuations around the correlation, we employ BBs. The BBs in each HAWC data set are obtained by following the procedure described in Section 3.4. The value of the $ncp_{\rm prior}$ parameter was set to $ncp_{\rm prior} = 9.5$ for both Mrk 501 and Mrk 421, corresponding to an FPR of 5%.

We only obtained five BBs that overlap with X-ray data, leading to a low statistics that will not be useful to study the correlation, although we did calculate it for completeness. However, in the case of Mrk 421, we identify twice the number of BBs compared to those reported by A. U. Abeysekara et al. (2017a). This increase is expected, given the extended duration of the analyzed data set, although the increase is probably not proportional to the amount of data added. However, this can be explained by the moderate and variable fluxes before 2017 April and for the only three distinct phases of higher activity, each of which was preceded by a period of low activity. In both LCs, longer BBs tend to absorb outliers due to the short-lived nature of emissions with the highest fluxes. Detailed information regarding the start and end time of these BBs for both Mrk 501 and Mrk 421 as well as the corresponding integrated γ-ray flux values >1 TeV is provided in Table 3. We are only showing BBs when the integrated flux significance was $>2\sigma$. Additionally, Figure 3 displays the BBs for both sources.

Using the BBs, we once again follow the procedure outlined in Section 3.3 to examine a linear correlation. The flux values reported in Table 3 are the integrated flux for the data within the BB, and both the flux normalization and the spectral index were set as free parameters. The results of this analysis are presented in Figure 4. Notably, the outliers are incorporated into the correlation through BBs with lower fluxes. As a consequence, the slopes of the correlations become less steep but remain consistent with the previously obtained values within twice their statistical uncertainties. Additionally, the values of b approach 0, although they still deviate from a 0 value.

4.4. Correlation Interpretation

In the case of Mrk 421, the intrinsic dispersion (σ_d) is slightly smaller than what was obtained using daily fluxes, but it remains significant and is of the same order of magnitude. Interestingly, the data dispersion increases as the fluxes increase. Specifically, the correlation is tighter for X-ray fluxes lower than 1.25 erg cm^{-2} s^{-1}, while for fluxes higher than 1.75 erg cm^{-2} s^{-1}, most of the data points deviate up to $3\sigma_d$ from the correlation. This could be indicative that the fluctuations are intrinsic to the source. However, this phenomenon is not observed in Mrk 501, possibly due to the lack of measured high-flux states in the data sample used.

According to the SSC model, for a single flare period, the expected correlation between X-ray and γ-ray fluxes is quadratic, and a change in particle density is responsible for the increase in the γ-ray flux (J. Kataoka et al. 1999; E. J. Lindfors et al. 2005; K. Katarzyński & K. Walczewska 2010). However, it has been demonstrated by several authors that this is not the case for Mrk 421 (M. Amenomori et al. 2003; M. Błażejowski et al. 2005; M. M. González et al. 2019; V. A. Acciari et al. 2020).

Mrk 421, in most observations, exhibits a linear correlation, and this linearity is generally attributed to contributions from multiple emission zones (K. Katarzyński & K. Walczewska 2010), external inverse Compton with seed photons from the

Table 3
Bayesian Blocks for HAWC fluxes

MJD Start	MJD Stop	Duration (days)	Flux >1 TeV ($\rm cm^{-2}\ s^{-1} \times 10^{-11}$)
		Mrk 501	
57076.42	57126.54	50.86	0.82 ± 0.22
57133.27	57250.20	117.68	0.64 ± 0.11
57251.94	57565.34	314.14	0.56 ± 0.09
57568.08	58093.89	528.55	0.15 ± 0.03
58097.63	59129.06	1031.18	0.07 ± 0.07
		Mrk 421	
56988.42	57045.52	57.842	2.55 ± 0.14
57046.26	57086.40	40.888	1.17 ± 0.14
57087.15	57143.25	56.844	2.45 ± 0.14
57144.00	57236.99	93.743	1.18 ± 0.11
57237.74	57239.99	2.992	7.07 ± 0.71
57240.73	57317.77	77.787	1.37 ± 0.11
57318.52	57368.63	50.861	0.21 ± 0.11
57369.38	57411.51	42.883	1.79 ± 0.15
57412.26	57529.19	117.678	0.49 ± 0.09
57529.94	57590.03	60.833	1.87 ± 0.14
57590.77	57753.58	163.552	0.17 ± 0.07
57754.33	57762.55	8.975	4.12 ± 0.38
57763.30	58105.61	343.061	1.19 ± 0.05
58106.36	58111.60	5.984	4.21 ± 0.44
58116.33	58132.54	16.954	3.28 ± 0.25
58133.29	58136.53	3.989	9.73 ± 0.65
58137.28	58150.49	13.962	3.72 ± 0.29
58151.24	58156.48	5.984	6.20 ± 0.48
58157.22	58212.32	57.842	2.51 ± 0.15
58215.07	58424.74	210.424	0.76 ± 0.07
58425.49	58556.38	131.640	1.36 ± 0.08
58557.13	58603.25	46.872	3.67 ± 0.16
58604.00	58766.81	163.552	1.52 ± 0.08
58767.55	58777.78	10.970	4.20 ± 0.43
58778.52	58915.40	137.623	0.85 ± 0.07
58916.14	59013.13	97.732	1.49 ± 0.10
59013.88	59022.11	9.973	6.45 ± 0.38
59023.85	59047.04	23.934	1.50 ± 0.22
59047.79	59054.02	6.981	5.74 ± 0.43
59054.77	59058.01	3.989	1.19 ± 0.46
59058.75	59060.00	2.992	5.53 ± 0.75
59061.75	59067.98	6.981	10.91 ± 0.50
59068.73	59070.97	2.992	6.35 ± 0.67
59071.72	59096.90	25.929	2.13 ± 0.22
59097.65	59100.89	3.989	9.78 ± 0.64
59101.64	59112.86	11.967	5.99 ± 0.37
59113.60	59127.82	14.959	2.72 ± 0.27
59128.56	59129.81	0.997	8.55 ± 0.85

Note. HAWC fluxes for 5 and 38 blocks found in the LCs of Mrk 501 and Mrk 421, respectively, when utilizing 2143 days of data and an FPR of 5% was chosen.

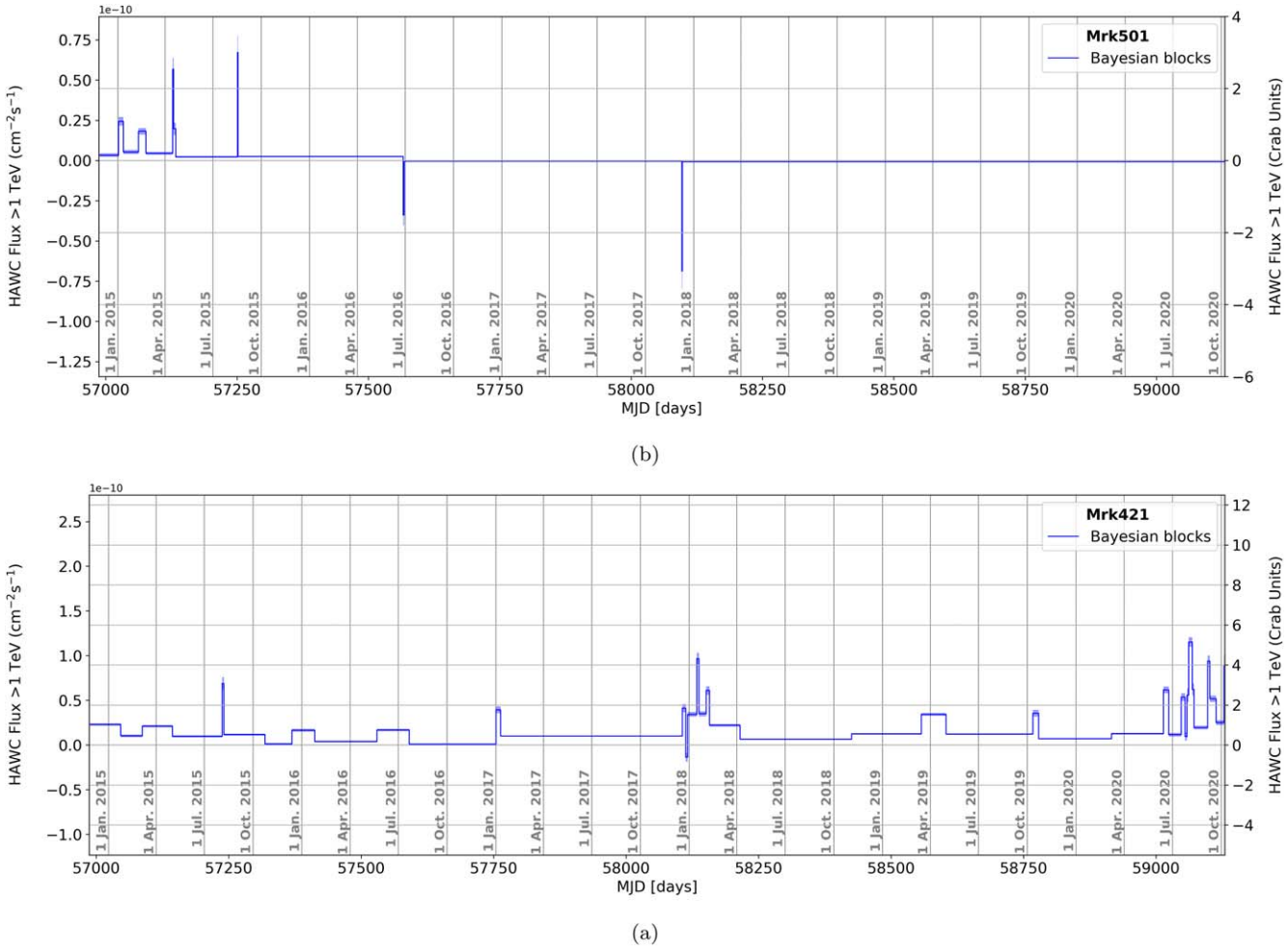

Figure 3. HAWC LCs for top panel (Mrk 501) and bottom panel (Mrk 421) for an integrated flux >1 TeV within the source transit (~6.2 hr) using a total of 2143 days after applying the BB algorithm.

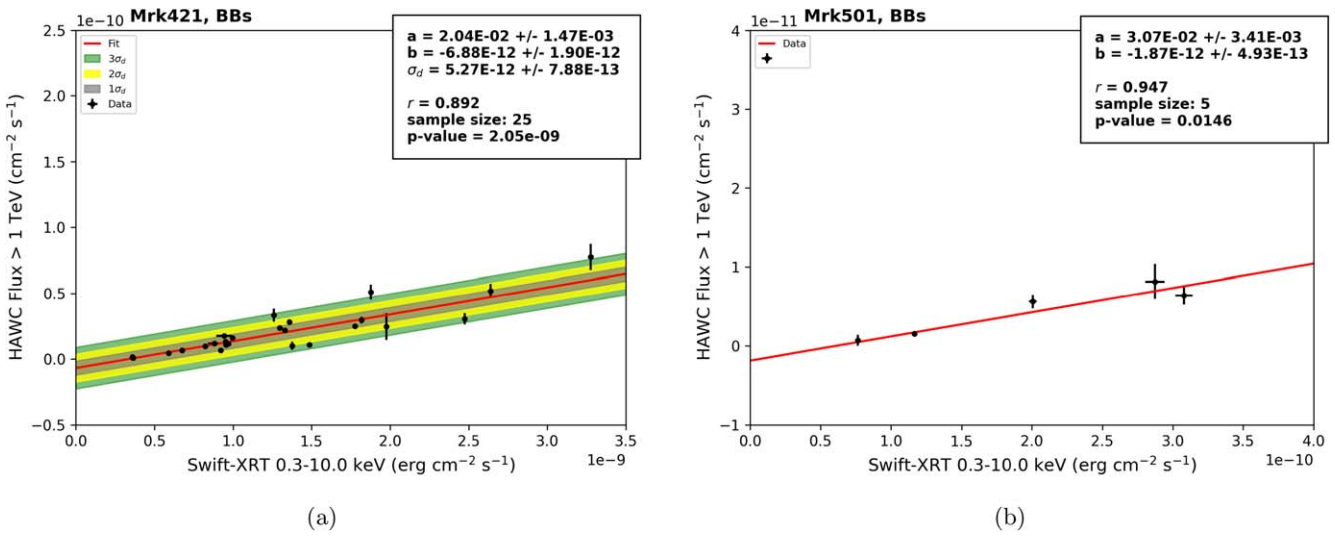

Figure 4. X-ray/γ-ray correlation for Mrk 421 in BBs (a). The p-value of the correlation is 0.892, which shows a strong consistency with a linear correlation. X-ray/γ-ray correlation for Mrk 501 in BBs (b). Due to the small size of the sample and the p-value, we only have evidence of a linear correlation.

accretion disk (C. D. Dermer et al. 1992), or emission from the central region of the blazar (M. Sikora et al. 1994). It may also result from emission in the Klein–Nishina energy regime (K. Katarzyński et al. 2005). For Mrk 421, depending on the model and activity state, the contribution to the TeV flux comes from photon scattering by the highest-energy electrons in the Klein–Nishina regime (F. Aharonian et al. 2005). Furthermore, most short-term TeV observations of Mrk 421 are consistent

with a one-zone scenario, as reported by A. A. Abdo et al. (2011), A. Arbet-Engels et al. (2021), and A. G. Markowitz et al. (2022), suggesting that there is no need for external photons.

On the contrary, it is evident that the HAWC data set presented here for Mrk 421 does not originate from a single flaring event; rather, it includes at least four well-separated flaring events during the long-term monitoring data spanning 6 yr. As noted in F. Aharonian et al. (2005), the long-term correlation is expected to differ from that of a single flaring event due to the inclusion of multiple flaring events, each driven by different processes that increase the TeV emission. These processes can include changes in particle densities or magnetic fields. The range of theoretical parameters describing flaring episodes at different multiwavelength campaigns suggests that multiple emission zones may be involved (A. Reimer et al. 2013; J. Aleksić et al. 2015b; T. Hovatta et al. 2015; R. Xue et al. 2019; A. Dmytriiev et al. 2021; R.-Y. Liu et al. 2023). Consequently, the long-term correlation can be seen as analogous to the correlation expected from multiple emission zones. Therefore, a linear correlation would be expected, as obtained in this work.

If we consider $F_\gamma \propto AF_X^\beta$, the total normalization of the correlation, represented by A, for a single flaring event depends strongly on the initial size of the blob, the initial particle density for electrons with energy above the break energy, and the initial magnetic field, as discussed in F. Aharonian et al. (2005). Therefore, assuming that these values vary slightly from flare to flare while remaining within the average values for a given blazar, we could expect the dispersion of the correlation to result from variations in these parameters.

4.5. γ-Ray Flux versus Photon Index

Previous analyses have reported a "harder-when-brighter" behavior in the relationship between spectral indices and their corresponding X-ray fluxes (B. Kapanadze et al. 2020), as well as in the relationship between the γ-fluxes and their corresponding spectral indices (V. A. Acciari et al. 2021). Since the synchrotron and SSC components are produced by the same electron population, we can expect their energy dependencies to be similar (B. Kapanadze et al. 2020).

We observed the same "harder-when-brighter" behavior for Mrk 421, as depicted in Figure 5(a). We employed the maximum-likelihood method, as discussed in Section 3.3, to establish the optimal linear representation of γ-ray fluxes observed by HAWC as a function of the corresponding spectral indices for the BBs displayed in Figure 3. We also depict the photon indices for the X-ray emission as function of the corresponding fluxes for Mrk 421 (panel (b)) and Mrk 501 (panel (c)). Although we observe a "harder-when-brighter" behavior on the X-ray fluxes for Mrk 421, it is far from being linear, consistent with the findings of B. Kapanadze et al. (2020).

In this work, we find that the γ-ray flux for Mrk 421 is negatively correlated to its photon index, with a PCC of -0.686 and a slope of $-3.07 \pm 0.42 \times 10^{-11}$. Unfortunately, no conclusion for Mrk 501 can be drawn due to its low activity during the studied period.

Two noteworthy points should be emphasized. First, the X-ray photon index remains relatively stable once the X-ray flux reaches approximately 1.1×10^{-9} erg cm^{-2} s^{-1} and 3×10^{-10} erg cm^{-2} s^{-1} for Mrk 421 and Mrk 501, respectively.

Second, in the case of Mrk 421, we observed a significant increase in the data dispersion around the best-fit correlation line. These deviations occur beyond the X-ray flux threshold of 1.1×10^{-9} erg cm^{-2} s^{-1}, with the emergence of outliers when using daily fluxes (Figure 2(a)) and when employing BBs (Figure 4 (a)). However, such behavior is not observed for Mrk 501, where all X-ray fluxes remain below 3×10^{-10} erg cm^{-2} s^{-1} (Figure 4(b)).

5. Conclusions

We investigated potential correlations between X-ray and γ-ray fluxes during a long-term monitoring study of Mrk 421 and Mrk 501, utilizing data from the HAWC Observatory. These two sources stand out as the brightest blazars observed by HAWC. Our data set included daily flux measurements spanning 2143 days, which is 4 times longer than the data set employed in the study by A. U. Abeysekara et al. (2017a). Instead of relying on Swift-BAT data for X-ray emissions, we opted for Swift-XRT data. This choice was motivated by the fact that Swift-XRT data cover an energy range closely aligned with the position of the synchrotron peak, similar to how the TeV energy range corresponds to the SSC peak for these two sources.

The HAWC LCs show that Mrk 501 maintained an extended low state for over 2 yr, as already reported by H. Abe et al. (2023), while Mrk 421 exhibited moderate variability throughout the 6 yr monitoring period, observed in both X-ray and γ-ray data. The most intense flares in each energy band occurred during distinct time periods, with a gap of more than 2 yr between them. However, it is worth noting that the source displayed simultaneous activity in both energy bands.

The daily flux data points reveal a long-term correlation for Mrk 421 for quasi-simultaneous observations; this correlation is well described by a linear relationship. For Mrk 501, we could not measure a correlation due to the low statistics obtained.

In Mrk 421, there exist outliers in the correlation, a finding in line with previous observations by M. M. González et al. (2019). However, the present study does not provide a definitive explanation for whether the correlation breaks down for γ-ray fluxes beyond a specific threshold or if other factors, such as the suppression of X-ray flux contributions from additional processes, influence γ-ray emissions. To delve into the origin of the dispersion in the correlation, we conducted an analysis employing BBs, as defined by the HAWC data. The results obtained indicate a moderate correlation for Mrk 501, and in the case of Mrk 421, a strong correlation was obtained, similar to the case of daily fluxes. Furthermore, these results imply that the dispersion observed about the line of best-fit correlation is intrinsic to the nature of these sources.

SSC models predict a quadratic correlation between X-ray and TeV emissions for individual flares. In these models, X-ray emission is attributed to synchrotron radiation from highly relativistic electrons within the jet, while TeV emission results from inverse-Compton scattering of synchrotron photons (A. A. Abdo et al. 2011). The presence of a linear correlation may be viewed as the collective effect of multiple emission zones, likely influenced by different processes throughout various flaring events within the time span considered in this study. Within this context, fluctuations observed around the

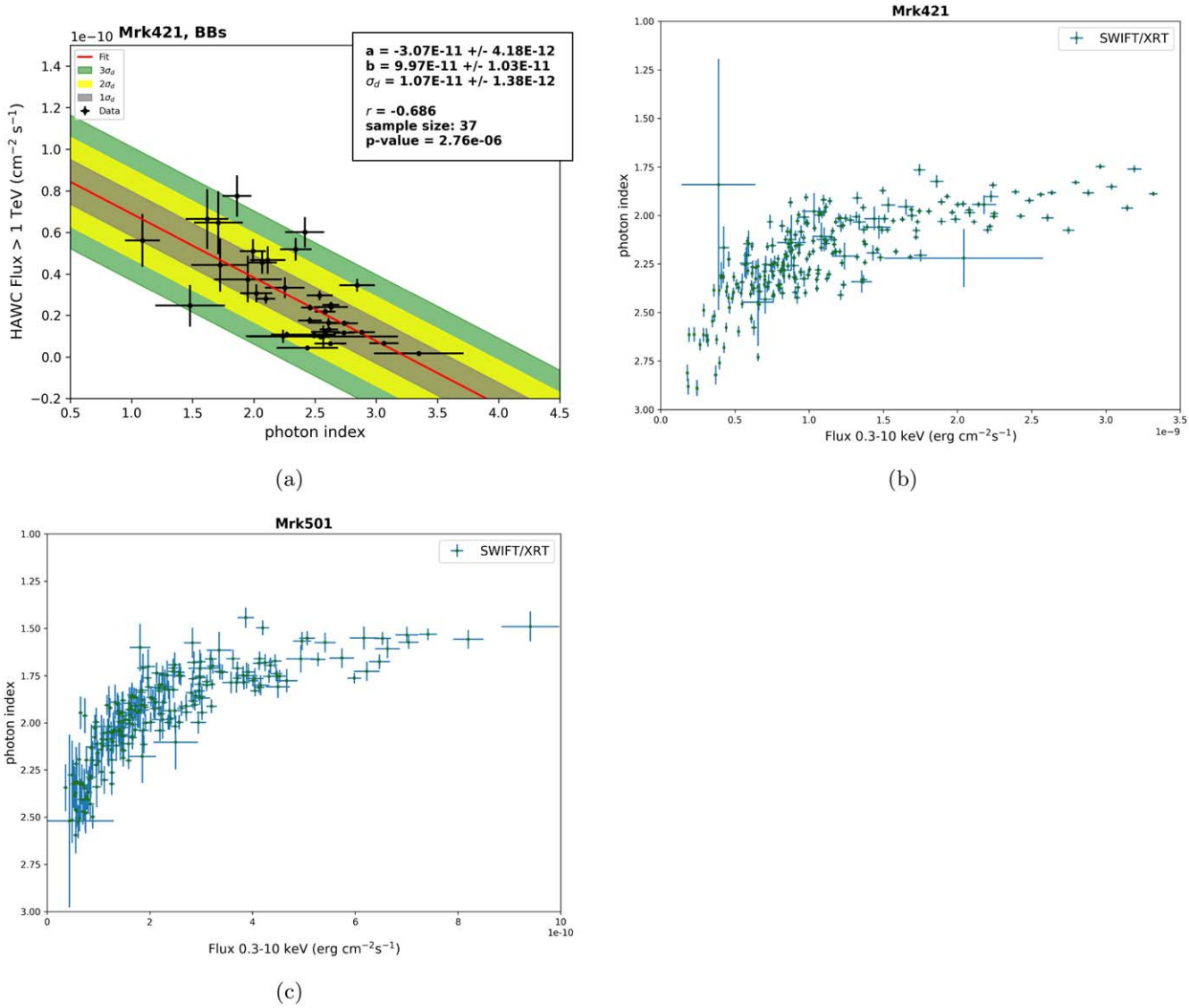

Figure 5. γ-ray flux vs. photon index (a) and photon index vs. X-ray flux ((b) and (c)). We observed a "harder-when-brighter" behavior for Mrk 421, revealing a linear relationship within the energy bands employed. However, in the case of the X-ray flux shown in (b), a linear correlation with the photon index is absent. Nevertheless, the "harder-when-brighter" trend observed in the γ-ray flux persists. Notably, X-ray flux values below 1.1×10^{-9} erg cm^{-2} s^{-1} correspond to γ-ray fluxes closer to the linear correlation displayed in Figure 2(a). For Mrk 501, a similar behavior to Mrk 421 is seen between the X-ray flux and the photon index, as depicted in (c). However, less dispersion is observed in the data for X-ray flux below 3×10^{-10}erg cm^{-2} s^{-1}.

correlation may be ascribed to slight deviations from the average values of specific parameters, including the initial size of the emission region, electron density above the break energy, and magnetic field strength.

A "harder-when-brighter" behavior is observed in the spectra of Mrk 421 within the two energy bands under consideration. Notably, the γ-ray flux exhibits a linear dependence on the photon index for Mrk 421, while the X-ray flux does not show a linear relationship with the corresponding photon index. As the photon index in the X-ray emission approaches its hardest value, the correlation appears to weaken. It is worth mentioning that the hardest photon index in the X-ray regime is not the same for the two sources.

This study reaffirms that the overall correlations for Mrk 421 and Mrk 501 are indeed linear, lending support to the leptonic model that involves multiple emission zones. Based on these findings, we can confidently assert that the harder-when-brighter behavior is firmly established in the γ-ray emission of Mrk 421.

Acknowledgments

We acknowledge the support from the US National Science Foundation (NSF); the US Department of Energy Office of High-Energy Physics; the Laboratory Directed Research and Development (LDRD) program of Los Alamos National Laboratory; Consejo Nacional de Ciencia y Tecnologìa (CONACyT), México, grants LNC-2023-117, 271051, 232656, 260378, 179588, 254964, 258865, 243290, 132197, A1-S-46288, A1-S-22784, CF-2023-I-645, cátedras 873, 1563, 341, 323, Red HAWC, México; DGAPA-UNAM grants IG101323, IN111716-3, IN111419, IA102019, IN106521, IN114924, IN110521, IN102223; VIEP-BUAP; PIFI 2012, 2013, PROFOCIE 2014, 2015; the University of Wisconsin Alumni Research Foundation; the Institute of Geophysics,

Planetary Physics, and Signatures at Los Alamos National Laboratory; Polish Science Center grant, DEC-2017/27/B/ST9/02272; Coordinación de la Investigación Cientìfica de la Universidad Michoacana; Royal Society—Newton Advanced Fellowship 180385; Generalitat Valenciana, grant CIDEGENT/2018/034; the Program Management Unit for Human Resources & Institutional Development, Research and Innovation, NXPO (grant No. B16F630069); Coordinación General Académica e Innovación (CGAI-UdeG), PRODEP-SEP UDG-CA-499; Institute of Cosmic Ray Research (ICRR), University of Tokyo. H.F. acknowledges support by NASA under award number 80GSFC21M0002. We also acknowledge the significant contributions over many years of Stefan Westerhoff, Gaurang Yodh, and Arnulfo Zepeda Domìnguez, all deceased members of the HAWC collaboration. Thanks to Scott Delay, Luciano Díaz, and Eduardo Murrieta for technical support.

ORCID iDs

R. Babu https://orcid.org/0000-0002-5529-6780
E. Belmont-Moreno https://orcid.org/0000-0003-3207-105X
K. Engel https://orcid.org/0000-0001-5737-1820
C. Espinoza https://orcid.org/0000-0001-7074-1726
J.A. García-González https://orcid.org/0000-0002-4188-5584
G. Luis-Raya https://orcid.org/0000-0003-2810-4867
P. Miranda-Romagnoli https://orcid.org/0000-0002-8390-9011
L. Nellen https://orcid.org/0000-0003-1059-8731
D. Rosa-González https://orcid.org/0000-0003-1327-0838
Abraham D. Falcone https://orcid.org/0000-0002-5068-7344

References

Abdalla, H., Aharonian, F., Benkhali, F., et al. 2019, ApJ, 870, 93
Abdo, A. A., Ackermann, M., Ajello, M., et al. 2011, ApJ, 736, 131
Abe, H., Abe, S., Acciari, V. A., et al. 2023, ApJS, 266, 37
Abeysekara, A., Albert, A., Alfaro, R., et al. 2023, NIMPA, 1052, 168253
Abeysekara, A. U., Albert, A., Alfaro, R., et al. 2017a, ApJ, 841, 100
Abeysekara, A. U., Albert, A., Alfaro, R., et al. 2017b, ApJ, 843, 39
Abeysekara, A. U., Albert, A., Alfaro, R., et al. 2019, ApJ, 881, 134
Acciari, V., Arlen, T., Aune, T., et al. 2014, APh, 54, 1
Acciari, V. A., Aliu, E., Aune, T., et al. 2009, ApJ, 703, 169
Acciari, V. A., Aliu, E., Arlen, T., et al. 2011, ApJ, 738, 25
Acciari, V. A., Ansoldi, S., Antonelli, L. A., et al. 2020, ApJS, 248, 29
Acciari, V. A., Ansoldi, S., Antonelli, L. A., et al. 2021, MNRAS, 504, 1427
Aharonian, F., Akhperjanian, A. G., Aye, K.-M., et al. 2005, A&A, 437, 95
Ajello, M., Atwood, W. B., Baldini, L., et al. 2017, ApJS, 232, 18
Albert, A., Alfaro, R., Alvarez, C., et al. 2022, ApJ, 929, 125
Albert, A., Alvarez, C., Camacho, J. R. A., et al. 2021, ApJ, 907, 67
Albert, J., Aliu, E., Anderhub, H., et al. 2007, ApJ, 663, 125
Aleksić, J., Ansoldi, S., Antonelli, L. A., et al. 2015a, A&A, 576, A126
Aleksić, J., Ansoldi, S., Antonelli, L. A., et al. 2015b, A&A, 578, A22
Amenomori, M., Ayabe, S., Cui, S. W., et al. 2003, ApJ, 598, 242
Arbet-Engels, A., Baack, D., Balbo, M., et al. 2021, A&A, 655, A93
Atkins, R., Benbow, W., Berley, D., et al. 2003, ApJ, 595, 803
Baloković, M., Paneque, D., Madejski, G., et al. 2016, ApJ, 819, 156
Bartoli, B., Bernardini, P., Bi, X. J., et al. 2012, ApJ, 758, 2
Bartoli, B., Bernardini, P., Bi, X. J., et al. 2016, ApJS, 222, 6
Błażejowski, M., Blaylock, G., Bond, I. H., et al. 2005, ApJ, 630, 130
Böttcher, M., Reimer, A., Sweeney, K., & Prakash, A. 2013, ApJ, 768, 54
Burrows, D. N., Hill, J. E., Nousek, J. A., et al. 2005, SSRv, 120, 165
Blazejowski, M., Blaylock, G., Bond, I. H., et al. 2005, ApJ, 630, 130
D'Agostini, G. 2003, RPPh, 66, 1383
D'Agostini, G. 2005, arXiv:physics/0511182
Dermer, C. D., Schlickeiser, R., & Mastichiadis, A. 1992, A&A, 256, L27
Dmytriiev, A., Sol, H., & Zech, A. 2021, MNRAS, 505, 2712
Edelson, R. A., & Krolik, J. H. 1988, ApJ, 333, 646
Falomo, R., Pian, E., & Treves, A. 2014, A&ARv, 22, 73
Fossati, G., Buckley, J., Edelson, R. A., Horns, D., & Jordan, M. 2004, NewAR, 48, 419
Fossati, G., Buckley, J. H., Bond, I. H., et al. 2008, ApJ, 677, 906
Garcìa-González, J. A., González, M. M., & Fraija, N. 2019, arXiv:1908.09452
Gehrels, N., Chincarini, G., Giommi, P., et al. 2004, ApJ, 611, 1005
Gliozzi, M., Sambruna, R. M., Jung, I., et al. 2006, ApJ, 646, 61
González, M. M., Patricelli, B., Fraija, N., & Garcìa-González, J. A. 2019, MNRAS, 484, 2944
HI4PI Collaboration, Ben Bekhti, N., Flöer, L., et al. 2016, A&A, 594, A116
Horan, D., Acciari, V. A., Bradbury, S. M., et al. 2009, ApJ, 695, 596
Hovatta, T., Petropoulou, M., Richards, J. L., et al. 2015, MNRAS, 448, 3121
Kapanadze, B., Dorner, D., Romano, P., et al. 2017, MNRAS, 469, 1655
Kapanadze, B., Gurchumelia, A., Dorner, D., et al. 2020, ApJS, 247, 27
Kataoka, J., Mattox, J. R., Quinn, J., et al. 1999, ApJ, 514, 138
Katarzyński, K., Ghisellini, G., Tavecchio, F., et al. 2005, A&A, 433, 479
Katarzyński, K., & Walczewska, K. 2010, A&A, 510, A63
Lindfors, E. J., Valtaoja, E., & Türler, M. 2005, A&A, 440, 845
Liu, R.-Y., Xue, R., Wang, Z.-R., Tan, H.-B., & Böttcher, M. 2023, MNRAS, 526, 5054
Macomb, D. J., Akerlof, C. W., Aller, H. D., et al. 1995, ApJL, 449, L99
MAGIC Collaboration, Acciari, V. A., Ansoldi, S., et al. 2020, A&A, 637, A86
MAGIC Collaboration, Acciari, V. A., Ansoldi, S., et al. 2021, A&A, 655, A89
Markowitz, A. G., Nalewajko, K., Bhatta, G., et al. 2022, MNRAS, 513, 1662
Martinez-Castellanos, I. 2019, arXiv:1908.06122
Padovani, P., & Giommi, P. 1995, ApJ, 444, 567
Pandey, A. 2020, Galax, 8, 55
Punch, M., et al. 1992, Natur, 358, 477
Quinn, J., Akerlof, C. W., Biller, S., et al. 1996, ApJL, 456, L83
Rebillot, P. F., Badran, H. M., Blaylock, G., et al. 2006, ApJ, 641, 740
Robertson, D. R. S., Gallo, L. C., Zoghbi, A., & Fabian, A. C. 2015, MNRAS, 453, 3455
Romano, P., Campana, S., Chincarini, G., et al. 2006, A&A, 456, 917
Scargle, J. D., Norris, J. P., Jackson, B., & Chiang, J. 2013, ApJ, 764, 167
Sikora, M., Begelman, M. C., & Rees, M. J. 1994, ApJ, 421, 153
Singh, K., Meintjes, P., Ramamonjisoa, F., & Tolamatti, A. 2019, NewA, 73, 101278
Stroh, M. C., & Falcone, A. D. 2013, ApJS, 207, 28
Tavecchio, F., Maraschi, L., & Ghisellini, G. 1998, ApJ, 509, 608
Tluczykont, M., Bernardini, E., Satalecka, K., et al. 2010, A&A, 524, A48
Ulrich, M.-H., Maraschi, L., & Urry, C. M. 1997, ARA&A, 35, 445
Xue, R., Liu, R.-Y., Petropoulou, M., et al. 2019, ApJ, 886, 23
Younk, P. W., Lauer, R. J., Vianello, G., et al. 2015, ICRC (The Hague), 34, 948